CHEMISTRY OF MATERIALS

pubs.acs.org/cm Article

Computational Discovery of Stable Heteroanionic Oxychalcogenides ABXO (A, B = Metals; X = S, Se, and Te) and Their Potential Applications

Jiangang He,* Zhenpeng Yao, Vinay I. Hegde, S. Shahab Naghavi, Jiahong Shen, Kyle M. Bushick, and Chris Wolverton*

Cite This: https://dx.doi.org/10.1021/acs.chemmater.0c01902 Read Online

ABSTRACT: Heteroanionic compounds that contain more than one type of anion have many unique and attractive properties, which make them desirable for numerous applications. However, because of challenges in synthesis and the complexity of their phase spaces, heteroanionic compounds are much less explored than more traditional homoanionic (single-anion) compounds. In this work, we perform a systematic screening for synthesizable, stable, heteroanionic oxysulfide, oxyselenide, and oxytelluride compounds ABXO (A and B are metals; X = S, Se, and Te) using high-throughput density functional theory calculations. 129 hitherto unknown ABXO compounds are predicted to be thermodynamically stable, therefore potentially synthesizable, and most of them are semiconductors. The calculated band gaps and other electronic and ionic properties are used to further screen potential compounds with promising applications such as thermoelectrics, transparent conductors, and solid-state electrolytes for Li/Na ion batteries. Our initial study on ABXO oxychalcogenides shows that heteroanionic compounds possess an extremely rich phase space with a variety of interesting properties and with a large number of these compounds still awaiting experimental synthesis.

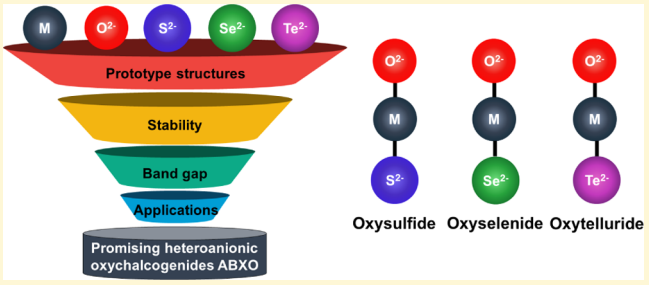

INTRODUCTION

In comparison to single-anion compounds such as oxides, chalcogenides, fluorides, and nitrides, compounds containing multiple anions (commonly referred to as "mixed-anion" or "heteroanionic") have not been widely studied.[1] However, many known heteroanionic compounds have various compelling properties, making them potential candidates for a wide variety of applications. For example, BiXO (X = Cl, Br, and I) and $LaTiNO_2$ are high-efficiency photocatalysts in the visible light region because of higher energy levels of X p orbitals than oxygen;[2,3] BiCuSeO and Bi_2SeO_2 have exciting thermoelectric (TE) performance;[4,5] the $Bi_4S_3O_4$ and LaFeAsO families of compounds show high-temperature superconductivity;[6,7] LaCuSO is an excellent p-type transparent conducting oxide (TCO);[8] Gd_2SO_2 has potential application in radiation detectors;[9] CaZnSO shows interesting piezo-luminescent properties;[10,11] and so forth.

The variation among anions in terms of properties such as the radius, mass, electronegativity, polarization, and oxidation state results in characteristics that are distinct from single-anion compounds. Heteroanionic compounds can also show interesting anion ordering behavior. Ordering a strongly ionic anion and a more covalent anion in a heteroanionic compound often leads to structures that are layered (natural heterostructures), have a local asymmetric coordination, and are globally non-centrosymmetry.[12,13] For example, the ZrCuSiAs-type structure (*P4/nmm* space group, see Figure 1a) is the most abundant crystal structure among ABXY (A and B are cations, and X and Y are anions) quaternary compounds,[14] for example, BiCuSeO, LaCoPO, LaCuSO, LaFeAsO, SrFeAsF, BaAgTeF, and SmCuSeF. This structure can be rationalized in terms of hard and soft (Lewis) acids and bases theory: soft (hard) acids form stronger bonds with soft (hard) bases.[15−17] The hard acid cation (Ba, Sr, La etc.) in this structure type bonds with the hard base anion (O and F) and forms anion-centered tetrahedra, while the less electropositive cation (Cu, Ag, Co, Fe, etc.) preferentially coordinates with the softer base (S, Se, As, Te, etc.), forming cation-centered tetrahedra.[18,19] If one cation in the structure is removed, it forms a ternary version of the ZrCuSiAs-type structure, which is the PrIO or PbClF-type structure with the *P4/nmm* space group (see Figure 1b). The ternary version is adopted by many AXY

Received: May 5, 2020
Revised: September 8, 2020
Published: September 9, 2020

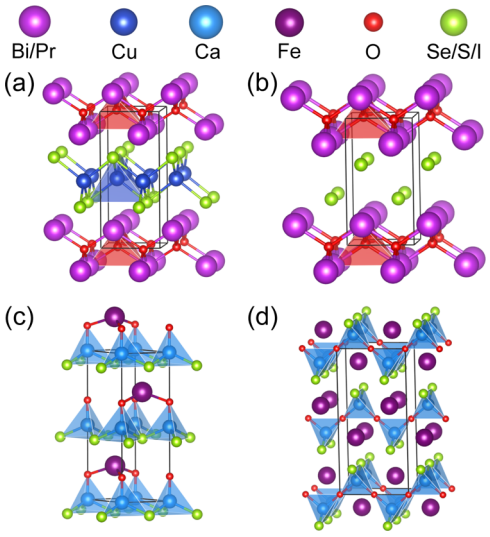

Figure 1. Commonly occurring crystal structure types in the ABXO family of heteroanionic compounds. (a) BiCuSeO ($ZrCuSiAs-CuHfSi_2$), (b) PrIO (PbClF), (c) CaZnSO, and (d) $ScRhSi_2$ (CaFeSeO). The cations in (a,b) structures have homoleptic coordinations and in (c,d) have heteroleptic coordinations.

heteroanionic compounds as well: BiIO, LaBrO, PbIF, ThIN, CaClF, and SrHI. Aside from the ZrCuSiAs-type, other structures with local or global non-centrosymmetric symmetry are commonly found in ABXY compounds as well. The SiC−4H (CaZnSO)-type structure ($P6_3mc$ space group, see Figure 1c), adopted by the heteroanionic compounds CaFeSO, CaZnSO, and ScAlCO, develops a permanent dipole moment along the crystallographic stacking direction because of anion ordering. In the CaZnSO-type structure, Zn is tetrahedrally coordinated with three S and one O atoms, and all ZnS_3O tetrahedra are corner-sharing in the *ab* plane and stacked along the *c* axis, separated by Ca cations.

Heteroanionic compounds are expected to provide a wider chemical space to search for new materials, and the extra degrees of freedom offered by the choice of multiple anions should allow for tuning of material properties.[1,20] Therefore, some inherent challenges in single-anion compounds could be alleviated by heteroanionic compounds. For example, band gaps of transition metal oxides can be significantly reduced by introducing less electronegative anions such as chalcogenides or pnictides, which boosts photocatalytic and photovoltaic efficiency by increasing visible-light absorption.[21,22] The redox potential of oxides can be enhanced by substituting oxygen with the more electronegative fluorine, potentially increasing the voltage of lithium ion batteries (LIBs).[23] Moreover, naturally forming superlattice structures in the heteroanionic family of compounds can be utilized to manipulate electron and phonon transport, for example, using quantum confinement effects or interlayer coupling, since the conducting and insulating layers are typically alternate in the superlattice.[24]

Owing to the challenges in synthesizing heteroanionic compounds and the complexity of the multianion chemical space, however, the number of known heteroanionic compounds is relatively small.[1] A significant acceleration in new heteroanionic materials discovery can be achieved by guiding experimental synthesis efforts using computational screening based on high-throughput (HT) calculations and machine learning.[25−30] HT computational screening-driven approaches, often based on materials properties computed with density functional theory (DFT), have been widely used to discover new synthesizable compounds for a wide variety of applications.[25−27,31−41]

In this work, we search for new, stable quaternary heteroanionic oxychalcogenide compounds with a simple equiatomic ABXO composition (A and B = metals, X = S, Se, or Te). We calculate several thousands of hypothetical compounds based on known structural prototypes and determine the ground-state structures at each composition. We identify thermodynamically stable phases by comparing their energies against all combinations of phases in the Open Quantum Materials Database (OQMD)[42] and verify their dynamic stability via phonon calculations. For newly identified thermodynamically stable or nearly stable phases, we calculate the electronic structure using the screened hybrid functional and perform separate screens for candidates suitable for three energy applications: TEs, transparent conductors, and Li/Na ion battery electrolytes. We find several promising candidates for each application and make recommendations for future experimental synthesis efforts.

METHODS

DFT Parameters. In this work, all DFT calculations are performed using the Vienna Ab Initio Simulation Package (VASP).[43,44] The Perdew−Burke−Ernzerhof (PBE) version of the exchange−correlation functional,[45] projector-augmented wave method[46,47] and the plane wave basis sets with an energy cutoff of 520 eV were used for structure relaxation, phonon calculations, and molecular dynamics (MD) simulation. Uniform *k*-point grids with a density of 6000−8000 *k*-points per reciprocal atom were used. Compounds made of elements with unfilled d-shells were spin-polarized, initialized in a ferromagnetic spin configuration, and the magnetic degree of freedom allowed to relax to self-consistency within a primitive unit cell. To avoid issues of convergence, pseudopotentials with f-electrons placed in the core were used for rare earth elements except the hybrid function band gap calculation for Ce-containing compounds. The effect of f-electrons on formation energies and convex hull distances of Ce^{3+} compounds is relatively small (see Note 1 of Supporting Information for more details). All parameters, including Hubbard *U* values,[48] were chosen to be consistent with those used for calculations in the OQMD (see ref 42 for details).

Chemical Space. In order to perform an efficient HT screening, only nominally charge-balanced ABXO (X = S, Se, and Te) compounds were calculated. Since the total oxidation state of XO is −4 (X^{2-} + O^{2-}), two possible ABXO combinations exist: $A^{1+}B^{3+}XO$ and $A^{2+}B^{2+}XO$. Therefore, only elements with possible nominal oxidation states of +1, +2, or +3 (Figure 2) are considered as cations in generating hypothetical heteroanionic compounds. We screened 972 $A^{1+}B^{3+}XO$ and 192 $A^{2+}B^{2+}XO$ compositions with 4 and 8 prototype structures, respectively. The prototype structures are from the ICSD and literature.

Thermodynamic *T* = 0 K Stability. The thermodynamic stability of a compound at 0 K is defined by its energetic distance from the convex hull of formation energies in the chemical space, that is, the difference in the formation energy of the compound and that of the lowest-energy linear combination of phases at that composition. Previous studies have shown that the distance to the convex hull of formation energies (often simply "convex hull distance" or "stability") is a reasonable metric of the likelihood of experimental synthesizability—a convex hull distance of zero or close to zero is a good indicator of its successful experimental synthesis.[49−51] All unique ordered phases in the OQMD (www.oqmd.org), a total of over 560,000 phases (as of June 2019), including ∼40,000 known compounds from the Inorganic Crystal Structure Database (ICSD)[52,53] and ∼500,000 hypothetical compounds based on common binary and ternary structure types,[54] were used for all

https://dx.doi.org/10.1021/acs.chemmater.0c01902
Chem. Mater. XXXX, XXX, XXX−XXX

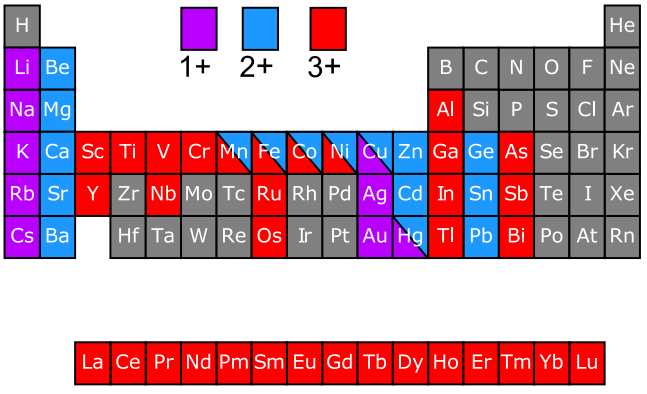

Figure 2. Elements from the periodic table used for substituting for A and B in ABXO heteroanionic compounds in this work. Gray elements are not considered in the HT calculations.

convex hull constructions. The hull distance (ΔE_h) of an ABXO compound is defined as the difference between its formation energy (ΔE) and the lowest-energy linear combination of phases in the A–B–X–O space with an overall composition of ABXO (sometimes referred to as "competing phases").

Crystal Structure Determination. To find the lowest energy structure at each unique composition, we use several approaches. We first use four and eight structure types as "prototypes" (commonly occurring in the ICSD or reported in the literature;[55] see Table 1) for

Table 1. Structure Type, Space Group, Polyhedron, the Number of Atoms per Primitive Cell (Z), and the Number of Compounds Reported in the ICSD within Our Chemical Space (N) of the Prototype Crystal Structures Used to Generate Hypothetical ABXO Compounds for Our HT Screening

structure type	space group	polyhedron composition	Z	N	source
		$A^{1+}B^{3+}XO$			
BiCuSeO	$P4/nmm$	OBi_4, $CuSe_4$	8	15	ICSD
LaCuSTe	$P2_1/c$	LaS_4Te_2, $CuSTe_3$	16	0	ICSD
LiAlSO	$Pmc2_1$	LiS_4O_2, AlO_2S_2	8	0	ref 55
LiAlSO	Pc	OLi_4, AlS	16	0	ref 55
		$A^{2+}B^{2+}XO$			
CaZnSO	$P6_3mc$	CaS_4O_3, ZnS_3O	8	2	ICSD
CaFeSeO	$Pnma$	$CaSe_4O_2$, $FeSe_2O_2$	16	1	ICSD
CaFeSeO	$Cmc2_1$	$CaSe_4O_2$, $FeSe_2O_2$	16	1	ICSD
LiSiNO	$P2_1/ab$	$LiNO_4$, SiN_3O	16	1	ICSD
AgHgIS	$P2_12_12_1$	AgS_2I_2, HgI	16	0	ICSD
SmCuTeS	$Pbca$	SmS_4Te_2, $CuTe_3S$	32	0	ICSD
BaZnSO	$Cmcm$	BaO_4, ZnO_2OS_2	8	2	ICSD
$BaNiS_2$	$P4/nmm$	BaO_5, NiS_4O	8	0	ICSD

$A^{1+}B^{3+}XO$ and $A^{2+}B^{2+}XO$, respectively, with A and B-substituted with elements from the periodic table according to their possible nominal oxidation states, as discussed earlier. In order to perform a more efficient screen, we substitute the cations of the prototype structure with the cations that have the same nominal oxidation state for $A^{1+}B^{3+}XO$. For $A^{2+}B^{2+}XO$, we generate two hypothetical structures for each prototype structure by alternating A^{2+} and B^{2+}. The hypothetical compounds are then computed within a HT-DFT framework using qmpy.[54] Further, for stable (ΔE_h = 0 meV/atom) and nearly stable (ΔE_h < 50 meV/atom) compounds with high symmetry (e.g., belonging to the $P4/nmm$ space group) but dynamic instability (i.e. with imaginary phonon frequencies), we generate low-symmetry (subgroup of the parent structure) structures by displacing atoms along the eigenvectors of the unstable phonon modes. An example of this process is shown in the Figure S1 and Table S1 of the Supporting Information. Finally, we use the particle swarm optimization (PSO) approach as implemented in the CALYPSO package[56,57] to perform global structure searches. We used CALPSO for a few selected compounds with promising applications rather than for the full HT search space because of the high cost of computing hours required.

Phonon Spectra and Lattice Thermal Conductivity. To check for dynamic stability of compounds and search for lower energy structures from unstable phonon modes, second-order force constants were computed by using the finite displacement method as implemented in the phonopy package.[58] Supercells with lattice constants more than 10 Å in all three lattice directions (e.g., 3 × 3 × 2 supercell for BiCuSeO-type structures) and an atomic displacement of 0.01 Å are utilized. The supercell size is large enough, and the atomic displacement is suitable to examine the lattice stabilities (see Supporting Information Figure S1 for the results of convergence tests). Lattice thermal conductivities were calculated by solving the Boltzmann transport equation for phonons, as implemented in the ShengBTE code,[59] based on the second- (4 × 4 × 2 supercell, 0.01 Å atomic displacement) and third-order (2 × 2 × 1 supercell, up to third–neighbor interactions) force constants calculated using phonopy and third-order.py,[60] respectively.

Electronic Transport. Electronic conductivities (σ) were calculated by solving the Boltzmann transport equation for electrons within a constant relaxation time approximation, as implemented in the Boltztrap package.[61] The electronic structure eigenvalues used in these calculations were computed with very dense k-meshes using the VASP package.[43,44] Electronic thermal conductivities (κ_e) were estimated using the Wiedemann–Franz law ($\kappa_e = L\sigma T$) with L = 2.45 × 10^{-8} WΩ K^{-2}.[62]

Electronic Structure, Band Gap, Effective Mass, and Branch Point Energy. The electronic band structures of all the stable/nearly stable compounds reported in this work are calculated using the PBE exchange–correlation functional. The screened hybrid functional HSE06[63] was used only to compute the minimum band gap from the density of states (DOS) of each compound. We note that although the standard screened hybrid functional HSE06, which uses a fixed exact exchange contribution of 25%, tends to underestimate (overestimate) the band gap of compounds with large (small) band gaps in general, it is a significant improvement over PBE in most cases.[64] The conductivity effective mass $(m_c^*)^{-1} = \sigma/ne^2\tau$ is calculated using the Boltztrap code within the constant relaxation time approximation as proposed by Gibbs et al. based on the PBE electronic structures.[65] The dopability of semiconductors is estimated by using the branch point energy (BPE),[66,67] which is calculated using the Matminer and pymatgen packages based on the HSE06 electronic structures.[68,69]

Cation Migration. To evaluate the alkali metal ion diffusivity in the selected heteroanionic compounds, we performed first-principles MD simulations as implemented in the VASP package.[43,44] Supercells of the selected heteroanionic compounds consisting of 24 formula units and Γ-point k-meshes were used, striking a balance between computational cost and accuracy. All MD simulations were performed in the canonical ensemble (NVT) using the Nosé thermostat[70,71] and velocity-verlet time integration scheme with a time step of 2 fs. Thermal expansion at each temperature was accounted by optimizing the supercell volume to minimize the average pressure (to zero) based on a series of short 1 ps runs.[72−74] Each system was heated from 100 K to the target temperature (600–1800 K) over 2 ps with 5 ps equilibration time. For diffusion runs, the MD simulations were performed for an additional 40 ps to ensure that no melting occurs.[74] The ionic diffusion behavior is calculated by a time-dependent mean square displacement (MSD)

$$\mathrm{MSD}(t) = \langle r^2(t)\rangle = \langle |r_i(t) - r_j(0)|^2\rangle \quad (1)$$

where $r_i(t)$ is the position of the ith Li^+/Na^+ at time t, and the average is over the time steps and all the Li^+/Na^+. According to the Einstein equation, the slope of the MSD is proportional to the diffusion coefficient D

https://dx.doi.org/10.1021/acs.chemmater.0c01902
Chem. Mater. XXXX, XXX, XXX–XXX

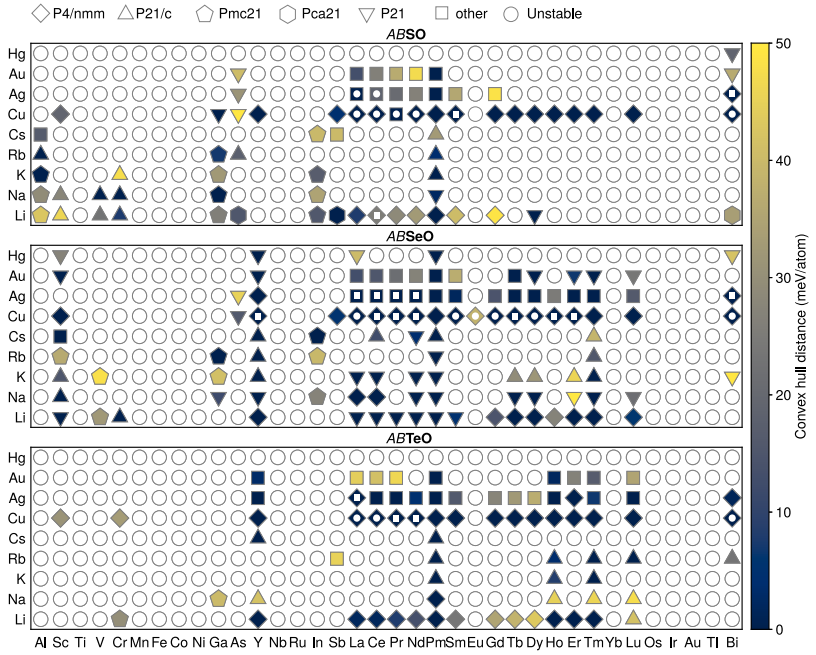

Figure 3. Heat map of the convex hull distance of $A^{1+}B^{3+}XO$ (X = S, Se, and Te) compounds. White unfilled circles indicate that the corresponding compound is unstable (ΔE_h > 50 meV/atom). Other shapes (e.g., diamond, square, triangle, etc.) represent the different symmetries of the respective ground-state structure (see the legend at the top of the figure). Small white circles and squares inside the larger shapes indicate that the compound has been reported in the ICSD and literature, respectively.

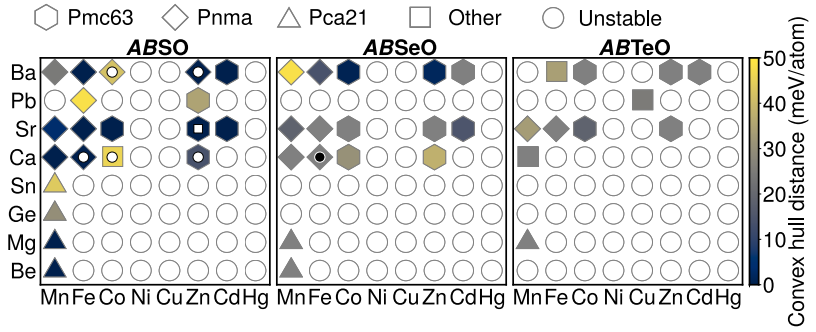

Figure 4. Heat map of the convex hull distance of $A^{2+}B^{2+}XO$ (X = S, Se, and Te) compounds. White unfilled circles indicate that the corresponding compound is unstable (ΔE_h > 50 meV/atom). Other shapes (e.g., diamond, square, triangle, etc.) represent the different symmetries of the respective ground-state structure (see legend at the top of the figure). Small white circles and squares inside the larger shapes indicate that the compound has been reported in the ICSD and literature, respectively.

$$D(t) = \frac{1}{6}\lim_{n\to\infty}\frac{\mathrm{d}}{\mathrm{d}t}\langle r^2(t)\rangle \quad (2)$$

Therefore, the activation energy barrier for Li^+/Na^+ diffusion can be extracted from the diffusion coefficients at various temperatures according to the Arrhenius equation[75]

$$\ln(D) = \ln(D_0) - E_{Act}/k_B T \quad (3)$$

where D_0 is the temperature-independent pre-exponential, E_{Act} is the activation barrier, and k_B is the Boltzmann constant. The electrochemical stability window of the stable compound NaGaSO is calculated following the method proposed by Richards et al.[76]

RESULTS AND DISCUSSION

Thermodynamic Stability at 0 K. The ground-state T = 0 K stability was calculated for each of the 972 $A^{1+}B^{3+}XO$ (192 $A^{2+}B^{2+}XO$) compositions in the chemical space, and each composition was sampled using 4 (8) structure types. We found 105 (24) stable and 119 (26) metastable compounds using our HT screening approach. Previous studies have shown that the distance to the convex hull of formation energies of a compound is a good estimate of the likelihood of its experimental synthesizability.[38,49−51,77,78] The thermodynamically stable (on the convex hull, ΔE_h = 0 meV/atom) and nearly stable (close to the convex hull, $\Delta E_h \leq$ 50 meV/atom) $A^{1+}B^{3+}XO$ and $A^{2+}B^{2+}XO$ compounds are summarized in Figures 3 and 4, respectively. We include nearly stable compounds to account for the following factors:

- The convex hull constructions performed in this work use 0 K formation energies of compounds. Therefore, entropic contributions (e.g., vibrational, electronic, configurational, and magnetic) to the thermodynamic stability of compounds are not included. Including entropic effects can lead to changes in the convex hull distances: for example, the low-temperature unstable compounds may become stable at high temperatures.[79,80]

https://dx.doi.org/10.1021/acs.chemmater.0c01902
Chem. Mater. XXXX, XXX, XXX−XXX

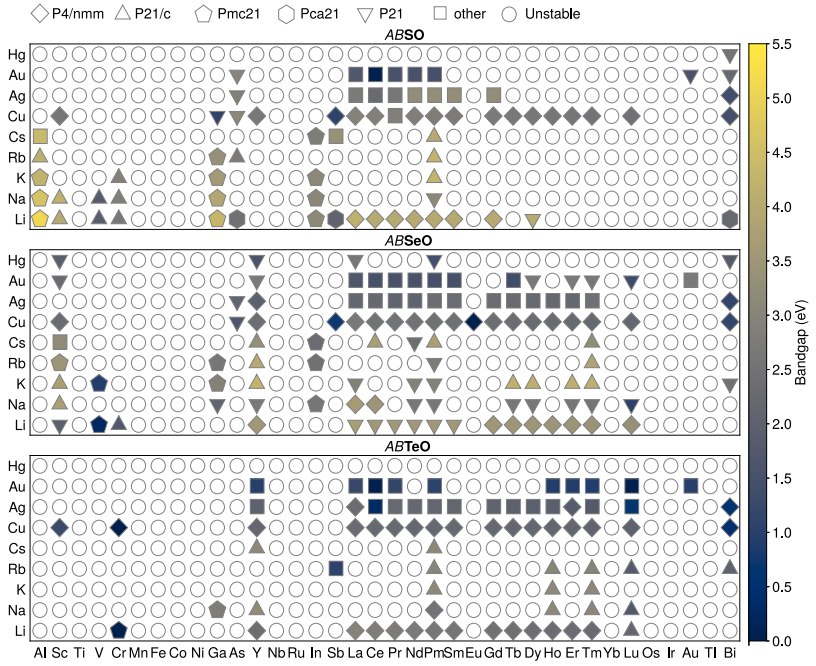

Figure 5. Heat map of the HSE06 band gaps of stable/nearly stable $A^{1+}B^{3+}XO$ (X = S, Se, and Te) compounds.

- A large number of experimentally synthesized and naturally occurring compounds are truly metastable and are often "kinetically stabilized" (i.e., trapped in a local but not global minimum of the energy)[77,78] For example, the energy difference between the ground-state structure and the observed, synthesized metastable polymorphs can be more than 50 meV/atom for oxides and around 50 meV/atom for sulfides and selenides.[77]
- Errors are associated with calculations of formation energies using DFT, for example, choice of exchange−correlation functionals, corrections to elemental reference chemical potentials, and so forth.[42,81] An important error especially associated with the heteroanionic compounds is from the Hubbard correction since the *U* parameters are typically applied to transition-metal cations and their *U* values are often extracted from single-anion compounds. However, these *U* corrections are typically only applied for certain anions (e.g. oxides). In the mixed anion homoleptic coordination, one might presume that no Hubbard *U* is actually required if the transition-metal cation bonds with a single anion that has low electronegativity. In the heteroleptic case, the *U* values extracted from the pure oxides or sulfides may be not suitable anymore. Moreover, the competing phases are mostly single-anion compounds (e.g., transition-metal oxides or transition-metal chalcogenides). It is very difficult to use a consistent *U* when computing the convex hull distance. We have studied the use of DFT + *U* in mixed anion systems in more detailed elsewhere.[82]
- Potentially lower energy structures were not found in our crystal structure search, for example, the true ground-state structures having large unit cells and/or very complex crystal structures.

However, there is in fact no strict upper limit of ΔE_h for synthesizability.[77,78] For example, although DFT can calculate the absolute vibrational entropy quite accurately,[83] the vibrational entropy could stabilize or destabilize a compound, depending on the phonon frequencies of all the involved phases. A small ΔE_h cutoff could miss some interesting metastable compounds, and a large ΔE_h will definitely lead to more false positive predictions. As shown in Figures 3 and 4 and Supporting Information Table S2, we found that all the experimentally reported oxychalcogenide compounds included in the ICSD or elsewhere in the literature are less than 50 meV/atom off the convex hull. Therefore, we used 50 meV/atom as the cutoff.

In addition to the experimentally reported compounds, we find more than 100 new, as-yet-unsynthesized oxychalcogenide compounds to be stable. During the preparation of this manuscript, two of our predicted compounds, BiAgSO and BiAgSeO, were synthesized and reported by other groups.[84,85] Since these two compounds were not included in the ICSD when we performed our HT-DFT screening, the successful discovery of these two compounds immediately validates two of our predictions and increases our confidence in the ability of our approach to predict entirely new, previously unreported, synthesizable ABXO compounds. In addition, we also find that the ground-state crystal structure identified by our approach is consistent with those reported in experiment for most compounds; that is, for all experimentally reported compounds, the lowest energy structure corresponds to the observed structure type. From Figure 3, we note that (i) many stable/nearly stable $A^+B^{3+}XO$ compounds contain rare earth elements (including Sc and Y), while most transition and post-transition metal-containing compounds are unstable (ΔE_h > 50 meV), (ii) the monovalent cations Cu^+ and Ag^+ are present in a large number of ABXO compounds, across all X elements (S, Se, and Te), and (iii) more stable/nearly stable compounds exist with Se^{2-} compared to Te^{2-} and S^{2-}. In general, all the above three observations are consistent with the experimental reports to date. Our phonon calculations indicate that some experimentally known *P*4/*nmm* compounds have small imaginary phonon frequencies and distorted structures obtained by displacing atoms along the eigenvectors of the unstable phonon modes have only slightly lower energies (few

https://dx.doi.org/10.1021/acs.chemmater.0c01902
Chem. Mater. XXXX, XXX, XXX−XXX

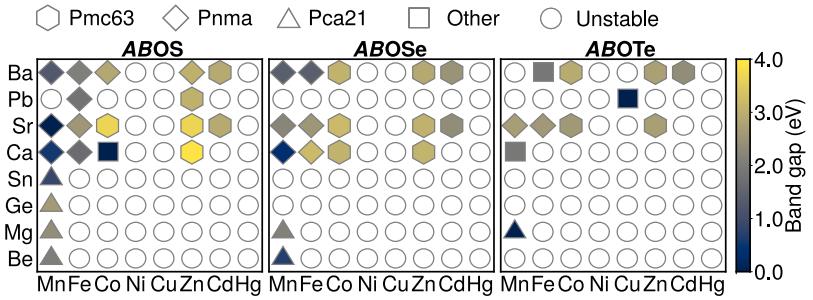

Figure 6. Heat map of the HSE06 band gaps of stable/nearly stable $A^{2+}B^{2+}XO$ (X = S, Se, and Te) compounds.

meV per atom) than the corresponding *P*4/*nmm* phases, indicating a weak instability of the *P*4/*nmm* phase at 0 K. This discrepancy is presumably because experimental reports usually correspond to room temperature or higher, which in some cases could be higher than the phase transition temperature. Also, we note that the choice of the exchange−correlation functional usually can have a significant large effect on phonon frequencies.[86] However, such a study is beyond the scope of this study. Our calculations also indicate that only Ba-, Sr-, and Ca-based compounds are thermodynamically stable when paired with a transition metal cation in the $A^{2+}B^{2+}XO$ family, consistent with prior experimental reports once again. Our calculations correctly reproduce all the synthesized $A^{2+}B^{2+}XO$ compounds to be on or close to the convex hull (ΔE_h < 50 meV/atom, see Figure 4).

In addition to reproducing the experimental results, we find many hitherto unknown ABXO compounds—Li^+, Ag^+, Sc^{3+}, Y^{3+}, Sr^{2+}, and Ba^{2+}-containing compounds in particular—that are thermodynamically stable/nearly stable. We note that despite being predicted to be thermodynamically stable, the experimental synthesis of many of these compounds may be challenging. For example, the only known example of a Li-containing ABXO compound, LiCeSO, was only very recently synthesized by inserting Li into CeSO using chemical or electrochemical methods.[87] BiAgSO and BiAgSeO were also only recently reported to be synthesized via ion exchange of Cu with Ag in pH- and T-controlled aqueous environments.[84,85]

Electronic Structure. The electronic structures and energy band gaps of the stable/nearly stable ABXO compounds are calculated to explore potential optoelectronic, TE, and photovoltaic applications. The electronic band structures are calculated at the PBE level of theory as it captures band dispersions reasonably accurately and is computationally affordable. However, PBE is well-known to underestimate the band gaps of semiconductors and insulators.[64,88] Hybrid functionals,[89] on the other hand, such as the screened hybrid functional HSE06,[63] are known to estimate band gaps in much better agreement with experimental values. Therefore, we use the HSE06 functional to calculate the band gap between the conduction band minimum (CBM) and valence band maximum (VBM) for every stable/nearly stable compound. The HSE06-calculated band gaps are summarized in Figures 5 and 6 for $A^+B^{3+}XO$ and $A^{2+}B^{2+}XO$, respectively. Most of the ABXO compounds are semiconductors, with band gaps up to 5.1 eV for the $A^{1+}B^{3+}XO$ and up to 4.0 eV for the $A^{2+}B^{2+}XO$ family of compounds. The calculated band gaps show a strong correlation with the electronegativity difference of the cations and anions in these compounds: (i) the band gap decreases from S to Se and to Te and (ii) the compounds containing alkali and alkaline-earth metal cations have larger band gaps than those containing transition metal and post-transition metal elements. LiAlSO (5.11 eV) and CaZnSO (3.90 eV, in good agreement with an experimental value of 3.7 eV[90]) have the largest band gap among $A^{1+}B^{3+}XO$ and $A^{2+}B^{2+}XO$ compounds, respectively. The sudden decrease of the band gap in Ce-containing compounds when crossing the rare-earth series is due to the appreciation of the f-electron in the Ce^{3+} ($4f^1$) cation. Note that except Ce-containing compounds, the band gaps reported here do not count the band gap formed by f-electrons of rare-earth cations since the f-electrons are treated as core electrons. The large range of band gaps in our predicted oxygenchalcogenide compounds enables us to explore further the energy and functional applications of these new semiconductors.

Thermoelectrics. TE materials have important applications in energy harvesting from waste heat, TE coolers, and thermal detectors as they can directly convert heat into electricity and vice versa. High-efficiency TE materials are required to compete with other technologies for practical applications. The TE efficiency is characterized by the figure of merit $zT = (S^2\sigma T)/(\kappa_L + \kappa_e)$, where S, σ, κ_e, κ_L, and T are the Seebeck coefficient, electrical conductivity, electronic thermal conductivity, lattice thermal conductivity, and temperature, respectively. In order to maximize zT, both electronic transport properties and lattice thermal conductivity have to be optimized carefully. However, S, σ, and κ ($\kappa_e + \kappa_L$) are usually coupled with each other. Although the TE materials based on oxides have potential advantages of low cost and high chemical stability at high temperatures compared to chalcogenides,[91] their zT is usually much lower than chalcogenides because of their higher κ_L and lower σ.[92] The combination of oxygen and a chalcogenide in a single compound provides an alternative solution that balances these factors.

The BiCuSeO oxychalcogenide has been found to have exciting TE properties.[4,93] Our HT search has identified several new candidate compounds that exhibit similar or even improved TE characteristics. The stability screening in the previous section suggests that BiAgSO and BiAgSeO are thermodynamically stable and BiAgTeO is nearly stable with a small convex hull distance (ΔE_h = 9 meV/atom). As mentioned before, BiAgSO and BiAgSeO have been synthesized recently.[84,85] Therefore, we believe BiAgTeO might be synthesizable with proper approaches as well. Our crystal structure search based on the prototype structure and PSO approaches indicates that the ZrCuSiAs-type structure is the lowest energy structure of BiAgSO, BiAgSeO, and BiAgTeO, which is isostructural with BiCuSeO—an excellent TE material at moderate temperatures.[4] The band gaps calculated by the screened hybrid functional HSE06 are 1.39,

https://dx.doi.org/10.1021/acs.chemmater.0c01902
Chem. Mater. XXXX, XXX, XXX−XXX

1.14, and 0.59 eV for BiAgSO, BiAgSeO, and BiAgTeO, respectively. Spin−orbit coupling (SOC) is not included in our HSE06 calculations because of the high computational cost. It could potentially lower the band gap by ∼0.2 eV for these compounds according to our PBEsol calculation. Note that band gaps of narrow band gap compounds, as observed in BiCuSeO (E_g = 0.8 eV) and other semiconductors, usually are slightly overestimated by HSE06 because the fixed Hartree−Fock mixture (25%) in the standard HSE06 is too high for small band gap compounds.[64] The experimentally measured band gaps of BiAgSO and BiAgSeO are 1.0 and 0.75 eV, respectively.[84,85] Therefore, it is reasonable to speculate that the band gap of BiAgTeO is 0.5 eV or lower. These results indicate that BiAgSeO and BiAgTeO possess suitable band gaps for high-performance TE materials, which usually are small band gap semiconductors as they demand high power factors (PFs) and low thermal conductivities concurrently.[94] A combined theoretical and experimental study on TE properties of BiAgSeO is reported elsewhere. Therefore, we only focus on BiAgTeO here.

Since accurate structural optimization is needed for phonon dispersion and transport calculations and the PBE functional cannot completely capture the long-range interactions between layers of the layered compounds with the ZrCuSiAs-type structure, here we use the PBEsol functional to study electron and phonon transport properties of BiAgTeO,[95] which has shown success with the similar compounds.[96,97] We compared the lattice constants of BiBXO (B = Cu and Ag; X = S and Se) compounds optimized by using several different exchange−correlation functionals and the experimental values. As shown in the Supporting Information Table S3, PBEsol reproduces the lattice constants of these compounds well. The PBEsol calculated band structures of BiAgTeO and BiCuSeO including SOC based on the fully relaxed crystal structures are shown in Figure 7. The VBM of BiCuSeO is located at the middle of the Σ line (the line between Γ and M points), which has a valley degeneracy of four, and the CBM is at the Z point with a valley degeneracy of one. The highly dispersive band with high valley degeneracy near the band edge is highly desirable for achieving a high PF (PF = σS^2, the product of electrical conductivity σ and the square of Seebeck coefficient S).[98,99] The small energy difference between the VBM and the second VBM at the Z point in BiCuSeO (26 meV) indicates that the second VBM can have non-negligible contribution at a high hole concentration. However, the band structure of BiAgTeO is different from BiCuSeO: the VBM is in the middle of the U line (the line between the Z and R points), which has a valley degeneracy of 4 as well, and the CBM is at the Γ point. The second VBM at the Z point almost has the same energy as the VBM, which can provide an additional contribution to enhance the PF. The semimetallic band structure of BiAgTeO is due to the band gap underestimation by the semilocal functional PBEsol. As we mentioned above, the HSE06-calculated band gap is 0.59 eV. These features of the electronic structure suggest that BiAgTeO could have comparable or even higher PF than BiCuSeO as long as they are properly doped. Therefore, we calculated the electrical transport properties of BiAgTeO and BiCuSeO based on first-principles electronic structures and semiempirical transport theory within the constant relaxation approximation (see Methods for details). The calculated electrical transport properties are displayed in Figure 8. For computational efficiency, we use the so-called reduced PF ($S^2\sigma/\tau$, τ is the electron relaxation time) to evaluate the electron transport properties of these compounds. BiAgTeO, as expected, has a much higher reduced PF within the layer stacking direction (⊥, perpendicular to the stacking direction) than that along the stacking direction (||, parallel to the stacking direction) because of the poor electrical conductivity along the stacking direction. Our results also demonstrate that BiAgTeO can have comparable or even higher PFs than BiCuSeO and SnSe (which has an ultrahigh PF[100]), assuming that the compound can be doped in the range of $10^{19} \sim 10^{20}$ cm^{-3} holes, provided these compounds have similar τ values.

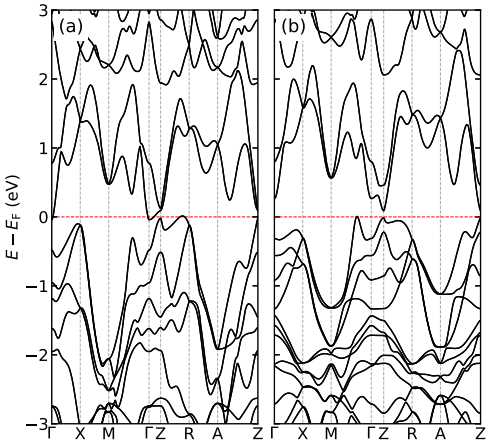

Figure 7. Band structures of BiAgTeO (a) and BiCuSeO (b) calculated by PBEsol, including spin−orbital coupling.

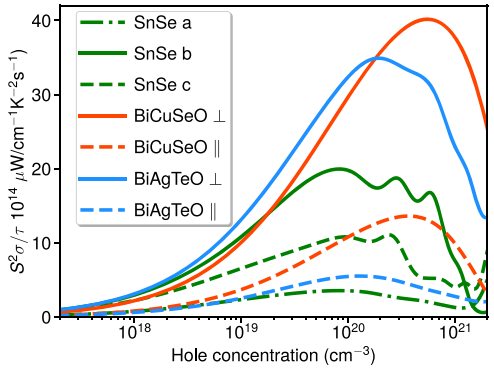

Figure 8. Reduced PFs ($S^2\sigma/\tau$) of BiAgTeO, BiCuSeO, and SnSe at 300 K. || and ⊥ are the directions parallel (out-of-the-plane) and perpendicular (in-plane) to the stacking layer, respectively.

A low lattice thermal conductivity (κ_L) is another desired property of high-efficiency TE materials since electron thermal conductivities (κ_e) in semiconductors are generally much smaller than κ_L.[101,102] Owing to a better agreement with experimental lattice constants of BiBXO compounds (B = Cu and Ag; X = S and Se), as shown in Table S3 of Supporting Information, the PBEsol functional is used to calculate the second- and third-order force constants of BiAgTeO, which are used to compute κ_L by solving the linearized phonon Boltzmann equation. The phonon dispersions, as shown in Figure 9, indicate that BiAgTeO is dynamically stable with softer phonon modes (lower phonon frequency) than BiCuSeO because of the larger atomic mass of Ag and Te and weaker bonding interactions in Ag−Te than Cu−Se, which

https://dx.doi.org/10.1021/acs.chemmater.0c01902
Chem. Mater. XXXX, XXX, XXX−XXX

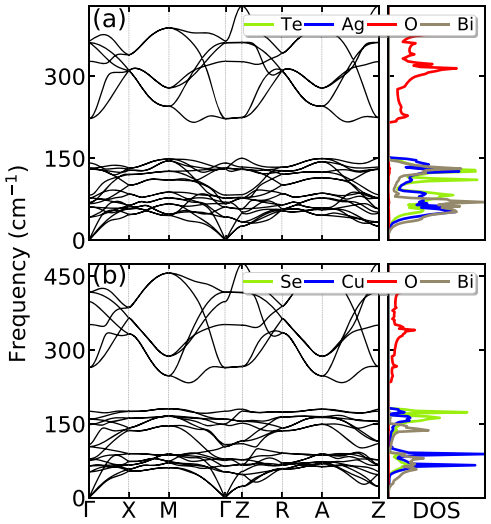

Figure 9. Phonon spectra and phonon DOS of BiAgTeO (a) and BiCuSeO (b).

implies a lower phonon velocity and therefore lower κ_L. Similar to Cu in BiCuSeO, Ag has a significant contribution to the flat phonon modes with low frequencies (see phonon DOS in Figure 9), which play important roles in scattering the heat-carrying phonon modes.[103] As seen in Figure 10, the calculated

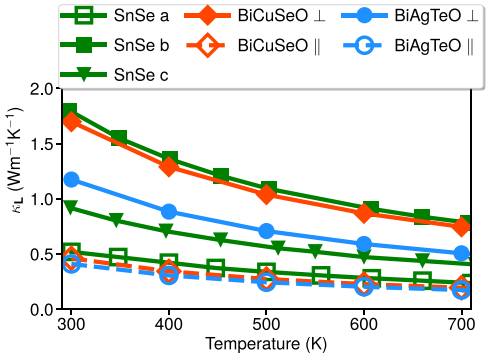

Figure 10. Lattice thermal conductivities of BiAgTeO and BiCuSeO in the directions parallel (out-of-the-plane, $\kappa_\parallel$) and perpendicular (in-plane, $\kappa_\perp$) to the stacking layer. The lattice thermal conductivities of SnSe are from the ref 104.

κ_L of BiAgTeO is lower than that of CuBiSeO, consistent with our analysis based on the phonon dispersion. The calculated κ_L is also lower than that of SnSe calculated by Carrete et al.,[104] which has an ultralow κ_L and high TE performance.[100,105] The low κ_L and high PF indicate that BiAgTeO is a promising heteroanion TE material.

The dopability is crucial for TE materials since a substantial conductivity can only be reached when the carrier concentration is high enough. The hole dopability of BiAgXO (X = S, Se, and Te) is roughly evaluated by using the BPE[66,67] (see Figure S3). The calculated BPE positions related to the middle of the band gap are similar to those of oxychalcogenides ACuXO (A = La and Bi; X = S, Se, and Te) and La_2SeO_2, which are p-type semiconductors. Therefore, it is expected that BiAgXO (X = S, Se, and Te) is hole-dopable.

Transparent Conductive Oxides. TCOs, which show both high optical transparency at the visible-light range and high electrical conductivity, are attractive materials for a large variety of applications such as solar cell contacts, electrochromic windows, flat panel displays, touchscreens, light emitting diodes, and a variety of other applications.[106,107] Although many good n-type TCOs (such as ZnO, SnO_2, and In_2O_3) have been discovered many years ago, good p-type TCOs are still missing. All the well-known p-type TCOs such as Cu_2O, $CuAlO_2$, $SrCu_2O_2$, and Rh_2ZnO_4 have either low conductivity or poor transparency.[108] One major issue of the p-type TCOs is the low electrical conductivity because the VBM in most oxides are from the localized and deep oxygen 2p orbitals, which leads to low carrier mobility (because of large hole effective masses) and low hole concentration.[109−112] In the past decades, many experimental and computational efforts have been put to search for good p-type TCOs.[108,112−117]

LaCuSO is one of the well-studied TCOs because of its large band gap (3.1 eV[8]) and small effective mass.[108] It also crystallizes in the ZrCuSiAs-type structure.[8] As shown in Figure 5, we find many oxysulfide compounds with wide band gaps ($E_g \geq 3.2$ eV), a first step in searching for new TCO materials. Another vital criteria of a high-performance TCO is a high electrical conductivity σ, which is a function of carrier concentration (n) and temperature (T). It is related to the carrier mobility $\mu(n, T)$ through $\sigma(n, T) = n(T)e\mu(n, T)$. Within the relaxation time approximation, the carrier mobility $\mu(n, T)$ is determined by the carrier lifetime/relaxation-time (τ) and the effective mass (m^*) at the band edge. Because of the high computational cost in computing τ limited by phonon scattering and the complexity of the band structure (beyond the parabola band approximation), we evaluate the electrical conductivity of $A^+B^{3+}XO$ compounds with band gaps larger than 3.2 eV using the so-called conductivity mass ($\bar{m}^*$) proposed by Gibbs et al.,[65] assuming that the carrier relaxation time (τ) is isotropic and all these compounds have similar τ

$$\bar{m}^*_{\alpha\beta}(n, T) = \frac{e^2\tau}{\sigma_{\alpha\beta}(n, T)}n(T)$$

where e is the electron charge. We use a carrier concentration of $n = 10^{18}$ cm^{-3} and $T = 300$ K to target the practical working conditions of a TCO. The relative value ($\bar{m}^*/\bar{m}^*_{LaCuSO}$) of the conductivity mass with respect to LaCuSO, which has smaller hole effective mass than many other oxides such as Cu_2O and $SrCu_2O_2$,[108] is used to get an estimate of the relative electrical transport solely because of the band structure. The calculated relative $\bar{m}^*$ of all the $A^+B^{3+}XO$ compounds with band gaps larger than 3.2 eV is shown in Figure 11. We found that the Se-

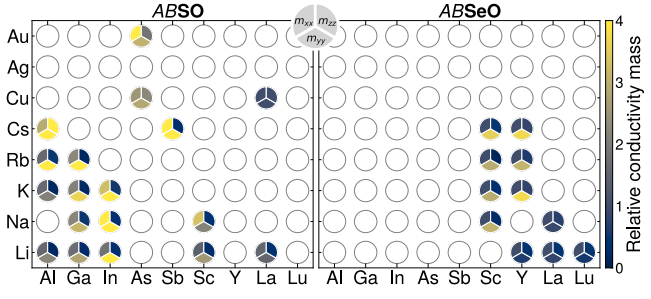

Figure 11. Transport hole effective masses of selected ABXO compounds with respect to LaCuSO at hole concentration of 10^{18} cm^{-3} and 300 K. Color indicates the effective mass of these compounds.

https://dx.doi.org/10.1021/acs.chemmater.0c01902
Chem. Mater. XXXX, XXX, XXX−XXX

based compounds YLiSeO, LaLiSeO, LuLiSeO, and NaLaSeO have a smaller conductivity mass than LaCuSO. They also have larger band gaps. Therefore, we suggest that these compounds are promising candidates for transparent conductive oxides.

Hole dopability is very important for p-type TCO. Again, we used BPE as a simple indicator of dopability.[67,115,118] Similar to the known p-type oxychalcogenides such as LaCuSO, LaCuSeO, BiCuSeO, and, $LaLa_2SeO_2$, the BPE of these compounds are close to the middle of the band gap, which implies that p-type doping is possible.

Superionic Conductors. Since the organic electrolytes have significant safety concerns of leakage and flammability,[119,120] solid-state electrolytes (SSEs) have been actively pursued for safe, energy-dense, and reversible storage of electrochemical energy in batteries.[121−123] Lithium and sodium superionic conductors are the main SSEs explored for solid-state LIBs and sodium ion batteries (SIBs).[124,125] Currently, the superionic conductors with ionic conductivities comparable to their organic liquid counterparts (10^{-2} S/cm) are generally sulfides (e.g. LGPS: $Li_{10}GeP_2S_{12}$ and NGPS: $Na_{10}GeP_2S_{12}$) and selenides.[124,126,127] However, sulfide- and selenide-based SSEs suffer from poor electrochemical stability.[128] On the contrary, oxide-based SSEs (e.g. LISICON: $Li_{2+2x}Zn_{1-x}GeO_4$, LLZO: $Li_7La_3Zr_2O_{12}$) are well-known for their high electrochemical stability and wide voltage window.[129,130]

Heteroanionic oxychalcogenide compounds are promising superionic conductors for SSEs in the LIBs and SIBs because of their potential to combine the merits of high ionic conductivity of sulfides/selenides and the remarkable electrochemical stability of oxides. Additionally, a large band gap (i.e., E_g > 3.5 eV) is favored for LIB and SIB applications to ensure that the electrolyte is electronically insulating. Therefore, stable and nearly stable oxysulfides and oxyselenides that have a large band gap and contain Li/Na are downselected to explore ionic conductivity for LIB and SIB applications. We conduct first-principles MD simulations to obtain Li/Na diffusion activation energies (see Methods for computational details). As shown in Figure 12, our calculated activation energies of many newly discovered ABXO compounds are comparable to the state-of-the-art Li/Na ion conductors such as $Li_{10}GeP_2S_{12}$ (LGPS, 0.24 eV),[124] garnet $Li_7La_3Zr_2O_{12}$ (0.25 eV),[131] and argyrodites $Li_{6+x}P_{1-x}Ge_xS_5I$ (0.24 eV).[132] The calculated electrochemical stability windows (V vs M/M^+) of NaGaSO, LiLaSeO, and LiNdSeO are 1.0−2.0, 0−1.9, and 0−1.8 eV, respectively.

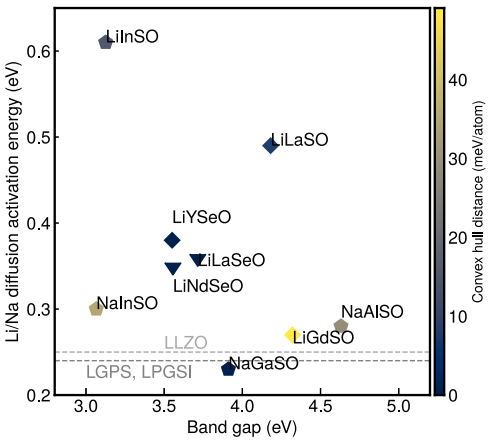

Figure 12. Activation energy of Li or Na diffusion as a function of HSE06 band gap for the selected heteroanionic compounds. The shape represents the symmetry of the compound, which is defined in Figure 5. The reference compounds are $Li_{10}GeP_2S_{12}$ (LGPS), garnet $Li_7La_3Zr_2O_{12}$ (LLZO), and LPGSI (argyrodites $Li_{6+x}P_{1x}Ge_xS_5I$).

Therefore, our top candidates are NaGaSO, NaAlSO, and LiGaSO with activation barriers of 0.23, 0.27, and 0.28 eV, respectively. We predict these compounds as candidates for SSEs in LIBs and SIBs, with superionic conductivity and a reasonably stable voltage window. We call for experimental validation of these predictions.

Synthesis Approaches. In general, heteroanionic compounds are more challenging to synthesize than single-anion compounds.[1] However, many oxychalcogenide compounds are actually prepared by classical solid-state reactions.[14] A number of other approaches also have been used to synthesize oxychalcogenide compounds, such as soft-chemistry,[133] solvothermal synthesis,[85,134,135] thin-film growth,[112] high-pressure synthesis,[136] ion exchange,[84] and topotactic reductive transformation.[87] Different approaches have to be chosen according to the properties of the precursors. DFT calculations also can assist experimental synthesis to find the best synthesis conditions. For example, the stability of a compound with respect to the chemical potential of elements and the Pourbaix diagram (if solvothermal method is used for synthesis) can be computed.[137,138]

CONCLUSIONS

In summary, the oxychalcogenide ABXO (X = S, Se, and Te) chemical space is systematically explored by using HT DFT calculations. More than one hundred unreported ABXO heteroanionic compounds are found to be thermodynamically stable or nearly stable. Electronic structure calculations show that most of these compounds are semiconductors with band gaps up to 5.1 eV, providing opportunities of finding new functional and energy materials with applications from TEs, to transparent conductors, to SSEs. Potential compounds are therefore screened according to their band gaps: the compounds with small band gaps (E_g < 0.8 eV) were investigated for TE applications; compounds with larger band gaps (E_g > 3.2 eV) are studied for transparent conductive oxides; and Li- or Na-based compounds with large band gaps (E_g > 3.0 eV) are investigated for the Li/Na solid electrolyte. More careful calculations of electron, phonon, and ion transport are performed for the selected compounds. Several new compounds with promising applications as TEs, transparent conductors, and SSEs are discovered. Our initial study on ABXO oxychalcogenides demonstrates the rich phase space and diverse physical properties of heteroanionic compounds, providing potential alternative solutions to alleviate challenges faced by single-anion materials. Our work opens up possibilities for accelerated design and synthesis of novel materials for a variety of applications.

ASSOCIATED CONTENT

Supporting Information

The Supporting Information is available free of charge at https://pubs.acs.org/doi/10.1021/acs.chemmater.0c01902.

Force constant convergence tests; an example of generating lower symmetry structures by freezing unstable phonon modes; a list of compounds within the 50 meV/atom above the convex hull; stabilities of compounds reported in the ICSD; branch energy points

https://dx.doi.org/10.1021/acs.chemmater.0c01902
Chem. Mater. XXXX, XXX, XXX−XXX

of selected compounds; and structure files (VASP POSCAR format) of studied compounds (ZIP)

Effect of *f*-electrons on formation energy and convex hull calculations; lattice constants of BiCuSO, BiCuSeO, BiAgSO, BiAgSeO, and BiAgTeO calculated with different exchange-correlation functionals (PDF)

AUTHOR INFORMATION

Corresponding Authors

Jiangang He − *Department of Materials Science and Engineering, Northwestern University, Evanston, Illinois 60208, United States;* orcid.org/0000-0001-9643-3617; Email: jiangang2020@gmail.com

Chris Wolverton − *Department of Materials Science and Engineering, Northwestern University, Evanston, Illinois 60208, United States;* orcid.org/0000-0003-2248-474X; Email: c-wolverton@northwestern.edu

Authors

Zhenpeng Yao − *Department of Materials Science and Engineering, Northwestern University, Evanston, Illinois 60208, United States; Department of Chemistry and Chemical Biology, Harvard University, Cambridge, Massachusetts 02138, United States;* orcid.org/0000-0001-8286-8257

Vinay I. Hegde − *Department of Materials Science and Engineering, Northwestern University, Evanston, Illinois 60208, United States;* orcid.org/0000-0003-4786-823X

S. Shahab Naghavi − *Department of Physical and Computational Chemistry, Shahid Beheshti University, Tehran 1983969411, Iran;* orcid.org/0000-0002-8511-2591

Jiahong Shen − *Department of Materials Science and Engineering, Northwestern University, Evanston, Illinois 60208, United States*

Kyle M. Bushick − *Department of Materials Science and Engineering, Northwestern University, Evanston, Illinois 60208, United States;* orcid.org/0000-0003-2089-1296

Complete contact information is available at: https://pubs.acs.org/10.1021/acs.chemmater.0c01902

Notes

The authors declare no competing financial interest.

ACKNOWLEDGMENTS

J.H. (HT DFT, phonon, electron and phonon transport calculations), C.W. (conceived and designed the project), and J.S. (HT DFT) acknowledge primary support via the National Science Foundation through the MRSEC program (NSF-DMR 1720139) at the Materials Research Center. Z.Y. (Li/Na diffusion) supported as a part of the Center for Electrochemical Energy Science, an Energy Frontier Research Center funded by the U.S. Department of Energy (DOS), office of Science, Basic Energy Science under award number DE-AC02-06CH11357. V.I.H. (HT DFT) acknowledges support from the Toyota Research Institute (TRI) through the Accelerated Materials Design and Discovery program. S.S.N. (HSE06 calculation) acknowledges financial assistance from award 70NANB14H012 from the U.S. Department of Commerce, National Institute of Standards and Technology as a part of the Center for Hierarchical Materials Design (CHiMaD). The authors acknowledge the computing resources provided by the National Energy Research Scientific Computing Center (NERSC), a U.S. Department of Energy Office of Science User Facility operated under contract no. DE-AC02-05CH11231 and the computational resources and staff contributions provided for the Quest high-performance computing facility at Northwestern University which is jointly supported by the Office of the Provost, the Office for Research, and Northwestern University Information Technology.

REFERENCES

(1) Kageyama, H.; Hayashi, K.; Maeda, K.; Attfield, J. P.; Hiroi, Z.; Rondinelli, J. M.; Poeppelmeier, K. R. Expanding frontiers in materials chemistry and physics with multiple anions. *Nat. Commun.* **2018**, *9*, 772.

(2) Ye, L.; Su, Y.; Jin, X.; Xie, H.; Zhang, C. Recent advances in BiOX (X= Cl, Br and I) photocatalysts: synthesis, modification, facet effects and mechanisms. *Environ. Sci.: Nano* **2014**, *1*, 90−112.

(3) Kasahara, A.; Nukumizu, K.; Takata, T.; Kondo, J. N.; Hara, M.; Kobayashi, H.; Domen, K. $LaTiO_2N$ as a visible-light (< 600 nm)-driven photocatalyst (2). *J. Phys. Chem. B* **2003**, *107*, 791−797.

(4) Zhao, L. D.; Berardan, D.; Pei, Y. L.; Byl, C.; Pinsard-Gaudart, L.; Dragoe, N. $Bi_{1-x}Sr_xCuSeO$ oxyselenides as promising thermoelectric materials. *Appl. Phys. Lett.* **2010**, *97*, 092118.

(5) Ruleova, P.; Drasar, C.; Lostak, P.; Li, C.-P.; Ballikaya, S.; Uher, C. Thermoelectric properties of Bi_2O_2Se. *Mater. Chem. Phys.* **2010**, *119*, 299−302.

(6) Nomura, T.; Kim, S. W.; Kamihara, Y.; Hirano, M.; Sushko, P. V.; Kato, K.; Takata, M.; Shluger, A. L.; Hosono, H. Crystallographic phase transition and high-Tc superconductivity in LaFeAsO: F. *Supercond. Sci. Technol.* **2008**, *21*, 125028.

(7) Mizuguchi, Y.; Fujihisa, H.; Gotoh, Y.; Suzuki, K.; Usui, H.; Kuroki, K.; Demura, S.; Takano, Y.; Izawa, H.; Miura, O. BiS_2-based layered superconductor $Bi_4O_4S_3$. *Phys. Rev. B: Condens. Matter Mater. Phys.* **2012**, *86*, 220510.

(8) Ueda, K.; Inoue, S.; Hirose, S.; Kawazoe, H.; Hosono, H. Transparent p-type semiconductor: LaCuOS layered oxysulfide. *Appl. Phys. Lett.* **2000**, *77*, 2701−2703.

(9) Rossner, W.; Ostertag, M.; Jermann, F. Properties and applications of gadolinium oxysulfide based ceramic scintillators. *Electrochemical Society Prceeedings*, 1999; pp 187−194.

(10) Tu, D.; Xu, C.-N.; Fujio, Y.; Yoshida, A. Mechanism of mechanical quenching and mechanoluminescence in phosphorescent CaZnOS: Cu. *Light: Sci. Appl.* **2015**, *4*, No. e356.

(11) Duan, C. J.; Delsing, A. C. A.; Hintzen, H. T. Photoluminescence properties of novel red-emitting Mn^{2+}-activated MZnOS (M= Ca, Ba) phosphors. *Chem. Mater.* **2009**, *21*, 1010−1016.

(12) Clarke, S. J.; Adamson, P.; Herkelrath, S. J. C.; Rutt, O. J.; Parker, D. R.; Pitcher, M. J.; Smura, C. F. Structures, physical properties, and chemistry of layered oxychalcogenides and oxypnictides. *Inorg. Chem.* **2008**, *47*, 8473−8486.

(13) Muir, S.; Subramanian, M. A. ZrCuSiAs type layered oxypnictides: A bird's eye view of LnMPnO compositions. *Prog. Solid State Chem.* **2012**, *40*, 41−56.

(14) Pöttgen, R.; Johrendt, D. Materials with ZrCuSiAs-type structure. *Z. Naturforsch. B* **2008**, *63*, 1135−1148.

(15) Pearson, R. G. Hard and soft acids and bases. *J. Am. Chem. Soc.* **1963**, *85*, 3533−3539.

(16) Pearson, R. G. Hard and soft acids and bases, HSAB, part 1: Fundamental principles. *J. Chem. Educ.* **1968**, *45*, 581.

(17) Pearson, R. G. Hard and soft acids and bases, HSAB, part II: Underlying theories. *J. Chem. Educ.* **1968**, *45*, 643.

(18) Luu, S. D. N.; Vaqueiro, P. Layered oxychalcogenides: structural chemistry and thermoelectric properties. *J Materiomics* **2016**, *2*, 131−140.

(19) Guittard, M.; Benazeth, S.; Dugue, J.; Jaulmes, S.; Palazzi, M.; Laruelle, P.; Flahaut, J. Oxysulfides and oxyselenides in sheets, formed by a rare earth element and a second metal. *J. Solid State Chem.* **1984**, *51*, 227−238.

(20) Harada, J. K.; Charles, N.; Poeppelmeier, K. R.; Rondinelli, J. M. Heteroanionic Materials by Design: Progress Toward Targeted Properties. *Adv. Mater.* **2019**, *31*, 1805295.
(21) Hitoki, G.; Takata, T.; Kondo, J. N.; Hara, M.; Kobayashi, H.; Domen, K. An oxynitride, TaON, as an efficient water oxidation photocatalyst under visible light irradiation ($\lambda \leq 500$ nm). *Chem. Commun.* **2002**, 1698−1699.
(22) Ishikawa, A.; Takata, T.; Kondo, J. N.; Hara, M.; Kobayashi, H.; Domen, K. Oxysulfide $Sm_2Ti_2S_2O_5$ as a stable photocatalyst for water oxidation and reduction under visible light irradiation (λ 650 nm). *J. Am. Chem. Soc.* **2002**, *124*, 13547−13553.
(23) Lee, J.; Kitchaev, D. A.; Kwon, D.-H.; Lee, C.-W.; Papp, J. K.; Liu, Y.-S.; Lun, Z.; Clément, R. J.; Shi, T.; McCloskey, B. D.; Guo, J.; Balasubramanian, M.; Ceder, G. Reversible Mn^{2+}/Mn^{4+} double redox in lithium-excess cathode materials. *Nature* **2018**, *556*, 185.
(24) Chen, H.; He, J.; Malliakas, C. D.; Stoumpos, C. C.; Rettie, A. J. E.; Bao, J.-K.; Chung, D. Y.; Kwok, W.-K.; Wolverton, C.; Kanatzidis, M. G. A Natural 2D Heterostructure $[Pb_{3.1}Sb_{0.9}S_4][Au_xTe_{2-x}]$ with Large Transverse Nonsaturating Negative Magnetoresistance and High Electron Mobility. *J. Am. Chem. Soc.* **2019**, *141*, 7544−7553.
(25) Hautier, G.; Fischer, C.; Ehrlacher, V.; Jain, A.; Ceder, G. Data mined ionic substitutions for the discovery of new compounds. *Inorg. Chem.* **2011**, *50*, 656−663.
(26) Wu, Y.; Lazic, P.; Hautier, G.; Persson, K.; Ceder, G. First principles high throughput screening of oxynitrides for water-splitting photocatalysts. *Energy Environ. Sci.* **2013**, *6*, 157−168.
(27) Curtarolo, S.; Hart, G. L. W.; Nardelli, M. B.; Mingo, N.; Sanvito, S.; Levy, O. The high-throughput highway to computational materials design. *Nat. Mater.* **2013**, *12*, 191−201.
(28) Meredig, B.; Agrawal, A.; Kirklin, S.; Saal, J. E.; Doak, J.; Thompson, A.; Zhang, K.; Choudhary, A.; Wolverton, C. Combinatorial screening for new materials in unconstrained composition space with machine learning. *Phys. Rev. B: Condens. Matter Mater. Phys.* **2014**, *89*, 094104.
(29) Ren, F.; Ward, L.; Williams, T.; Laws, K. J.; Wolverton, C.; Hattrick-Simpers, J.; Mehta, A. Accelerated discovery of metallic glasses through iteration of machine learning and high-throughput experiments. *Sci. Adv.* **2018**, *4*, No. eaaq1566.
(30) Schleder, G. R.; Acosta, C. M.; Fazzio, A. Exploring Two-Dimensional Materials Thermodynamic Stability via Machine Learning. *ACS Appl. Mater. Interfaces* **2019**, *12*, 20149−20157.
(31) Sanvito, S.; Oses, C.; Xue, J.; Tiwari, A.; Zic, M.; Archer, T.; Tozman, P.; Venkatesan, M.; Coey, M.; Curtarolo, S. Accelerated discovery of new magnets in the Heusler alloy family. *Sci. Adv.* **2017**, *3*, No. e1602241.
(32) Tabor, D. P.; Roch, L. M.; Saikin, S. K.; Kreisbeck, C.; Sheberla, D.; Montoya, J. H.; Dwaraknath, S.; Aykol, M.; Ortiz, C.; Tribukait, H.; Amador-Bedolla, C.; Brabec, C. J.; Maruyama, B.; Persson, K. A.; Aspuru-Guzik, A. Accelerating the discovery of materials for clean energy in the era of smart automation. *Nat. Rev. Mater.* **2018**, *3*, 5−20.
(33) Kirklin, S.; Saal, J. E.; Hegde, V. I.; Wolverton, C. High-throughput computational search for strengthening precipitates in alloys. *Acta Mater.* **2016**, *102*, 125−135.
(34) Carrete, J.; Li, W.; Mingo, N.; Wang, S.; Curtarolo, S. Finding unprecedentedly low-thermal-conductivity half-Heusler semiconductors via high-throughput materials modeling. *Phys. Rev. X* **2014**, *4*, 011019.
(35) Nyshadham, C.; Oses, C.; Hansen, J. E.; Takeuchi, I.; Curtarolo, S.; Hart, G. L. W. A computational high-throughput search for new ternary superalloys. *Acta Mater.* **2017**, *122*, 438−447.
(36) He, J.; Amsler, M.; Xia, Y.; Naghavi, S. S.; Hegde, V. I.; Hao, S.; Goedecker, S.; Ozoliņš, V.; Wolverton, C. Ultralow thermal conductivity in full Heusler semiconductors. *Phys. Rev. Lett.* **2016**, *117*, 046602.
(37) He, J.; Naghavi, S. S.; Hegde, V. I.; Amsler, M.; Wolverton, C. Designing and discovering a new family of semiconducting quaternary heusler compounds based on the 18-electron rule. *Chem. Mater.* **2018**, *30*, 4978−4985.
(38) Gautier, R.; Zhang, X.; Hu, L.; Yu, L.; Lin, Y.; Sunde, T. O. L.; Chon, D.; Poeppelmeier, K. R.; Zunger, A. Prediction and accelerated laboratory discovery of previously unknown 18-electron ABX compounds. *Nat. Chem.* **2015**, *7*, 308.
(39) Cai, Y.; Xie, W.; Teng, Y. T.; Harikesh, P. C.; Ghosh, B.; Huck, P.; Persson, K. A.; Mathews, N.; Mhaisalkar, S. G.; Sherburne, M.; Asta, M. High-throughput Computational Study of Halide Double Perovskite Inorganic Compounds. *Chem. Mater.* **2019**, *31*, 5392−5401.
(40) Dagdelen, J.; Montoya, J.; de Jong, M.; Persson, K. Computational prediction of new auxetic materials. *Nat. Commun.* **2017**, *8*, 323.
(41) Yao, Z.; Hegde, V. I.; Aspuru-Guzik, A.; Wolverton, C. Discovery of Calcium-Metal Alloy Anodes for Reversible Ca-Ion Batteries. *Adv. Energy Mater.* **2019**, *9*, 1802994.
(42) Kirklin, S.; Saal, J. E.; Meredig, B.; Thompson, A.; Doak, J. W.; Aykol, M.; Rühl, S.; Wolverton, C. The Open Quantum Materials Database (OQMD): assessing the accuracy of DFT formation energies. *npj Comput. Mater.* **2015**, *1*, 15010.
(43) Kresse, G.; Furthmüller, J. Efficient iterative schemes for ab-initio total-energy calculations using a plane-wave basis set. *Phys. Rev. B: Condens. Matter Mater. Phys.* **1996**, *54*, 11169−11186.
(44) Kresse, G.; Furthmüller, J. Efficiency of ab-initio total energy calculations for metals and semiconductors using a plane-wave basis set. *Comput. Mater. Sci.* **1996**, *6*, 15−50.
(45) Perdew, J. P.; Burke, K.; Ernzerhof, M. Generalized Gradient Approximation Made Simple. *Phys. Rev. Lett.* **1996**, *77*, 3865−3868.
(46) Blöchl, P. E. Projector augmented-wave method. *Phys. Rev. B: Condens. Matter Mater. Phys.* **1994**, *50*, 17953−17979.
(47) Kresse, G.; Joubert, D. From ultrasoft pseudopotentials to the projector augmented-wave method. *Phys. Rev. B: Condens. Matter Mater. Phys.* **1999**, *59*, 1758−1775.
(48) Dudarev, S. L.; Botton, G. A.; Savrasov, S. Y.; Humphreys, C. J.; Sutton, A. P. Electron-energy-loss spectra and the structural stability of nickel oxide: An LSDA+ U study. *Phys. Rev. B: Condens. Matter Mater. Phys.* **1998**, *57*, 1505.
(49) Ma, J.; Hegde, V. I.; Munira, K.; Xie, Y.; Keshavarz, S.; Mildebrath, D. T.; Wolverton, C.; Ghosh, A. W.; Butler, W. H. Computational investigation of half-Heusler compounds for spintronics applications. *Phys. Rev. B* **2017**, *95*, 024411.
(50) Ma, J.; He, J.; Mazumdar, D.; Munira, K.; Keshavarz, S.; Lovorn, T.; Wolverton, C.; Ghosh, A. W.; Butler, W. H. Computational investigation of inverse Heusler compounds for spintronics applications. *Phys. Rev. B* **2018**, *98*, 094410.
(51) Emery, A. A.; Saal, J. E.; Kirklin, S.; Hegde, V. I.; Wolverton, C. High-throughput computational screening of perovskites for thermochemical water splitting applications. *Chem. Mater.* **2016**, *28*, 5621−5634.
(52) Bergerhoff, G.; Brown, I. D. Crystallographic databases. *Int. Union Crystallogr.* **1987**, *360*, 77−95.
(53) Belsky, A.; Hellenbrandt, M.; Karen, V. L.; Luksch, P. New developments in the Inorganic Crystal Structure Database (ICSD): accessibility in support of materials research and design. *Acta Crystallogr. B* **2002**, *58*, 364−369.
(54) Saal, J. E.; Kirklin, S.; Aykol, M.; Meredig, B.; Wolverton, C. Materials Design and Discovery with High-Throughput Density Functional Theory: The Open Quantum Materials Database (OQMD). *J. Oper. Manag.* **2013**, *65*, 1501−1509.
(55) Wang, X.; Xiao, R.; Li, H.; Chen, L. Oxysulfide LiAlSO: A Lithium Superionic Conductor from First Principles. *Phys. Rev. Lett.* **2017**, *118*, 195901.
(56) Wang, Y.; Lv, J.; Zhu, L.; Ma, Y. Crystal structure prediction via particle-swarm optimization. *Phys. Rev. B: Condens. Matter Mater. Phys.* **2010**, *82*, 094116.
(57) Wang, Y.; Lv, J.; Zhu, L.; Ma, Y. CALYPSO: A method for crystal structure prediction. *Comput. Phys. Commun.* **2012**, *183*, 2063−2070.
(58) Togo, A.; Oba, F.; Tanaka, I. First-principles calculations of the ferroelastic transition between rutile-type and $CaCl_2$-type SiO_2 at high

https://dx.doi.org/10.1021/acs.chemmater.0c01902
Chem. Mater. XXXX, XXX, XXX−XXX

pressures. *Phys. Rev. B: Condens. Matter Mater. Phys.* **2008**, *78*, 134106.
(59) Li, W.; Carrete, J.; A. Katcho, N.; Mingo, N. ShengBTE: a solver of the Boltzmann transport equation for phonons. *Comput. Phys. Commun.* **2014**, *185*, 1747−1758.
(60) Li, W.; Lindsay, L.; Broido, D. A.; Stewart, D. A.; Mingo, N. Thermal conductivity of bulk and nanowire $Mg_2Si_xSn_{1-x}$ alloys from first principles. *Phys. Rev. B: Condens. Matter Mater. Phys.* **2012**, *86*, 174307.
(61) Madsen, G. K. H.; Singh, D. J. BoltzTraP. A code for calculating band-structure dependent quantities. *Comput. Phys. Commun.* **2006**, *175*, 67−71.
(62) Franz, R.; Wiedemann, G. Ueber die Wärme-Leitungsfähigkeit der Metalle. *Ann. Phys. Chem.* **1853**, *165*, 497−531.
(63) Heyd, J.; Scuseria, G. E.; Ernzerhof, M. Hybrid functionals based on a screened Coulomb potential. *J. Chem. Phys.* **2003**, *118*, 8207−8215.
(64) He, J.; Franchini, C. Assessing the performance of self-consistent hybrid functional for band gap calculation in oxide semiconductors. *J. Condens. Matter Phys.* **2017**, *29*, 454004.
(65) Gibbs, Z. M.; Ricci, F.; Li, G.; Zhu, H.; Persson, K.; Ceder, G.; Hautier, G.; Jain, A.; Snyder, G. J. Effective mass and Fermi surface complexity factor from ab initio band structure calculations. *npj Comput. Mater.* **2017**, *3*, 8.
(66) Tersoff, J. Theory of semiconductor heterojunctions: The role of quantum dipoles. *Phys. Rev. B: Condens. Matter Mater. Phys.* **1984**, *30*, 4874.
(67) Schleife, A.; Fuchs, F.; Rödl, C.; Furthmüller, J.; Bechstedt, F. Branch-point energies and band discontinuities of III-nitrides and III-/II-oxides from quasiparticle band-structure calculations. *Appl. Phys. Lett.* **2009**, *94*, 012104.
(68) Ward, L.; et al. Matminer: An open source toolkit for materials data mining. *Comput. Mater. Sci.* **2018**, *152*, 60−69.
(69) Ong, S. P.; Richards, W. D.; Jain, A.; Hautier, G.; Kocher, M.; Cholia, S.; Gunter, D.; Chevrier, V. L.; Persson, K. A.; Ceder, G. Python Materials Genomics (pymatgen): A robust, open-source python library for materials analysis. *Comput. Mater. Sci.* **2013**, *68*, 314−319.
(70) Nosé, S. A unified formulation of the constant temperature molecular dynamics methods. *J. Chem. Phys.* **1984**, *81*, 511−519.
(71) Nosé, S. Constant temperature molecular dynamics methods. *Prog. Theor. Phys. Suppl.* **1991**, *103*, 1−46.
(72) Bin, H.; Yao, Z.; Zhu, S.; Zhu, C.; Pan, H.; Chen, Z.; Wolverton, C.; Zhang, D. A high-performance anode material based on $FeMnO_3$/graphene composite. *J. Alloys Compd.* **2017**, *695*, 1223−1230.
(73) Li, Q.; Liu, H.; Yao, Z.; Cheng, J.; Li, T.; Li, Y.; Wolverton, C.; Wu, J.; Dravid, V. P. Electrochemistry of selenium with sodium and lithium: kinetics and reaction mechanism. *ACS Nano* **2016**, *10*, 8788−8795.
(74) Farrell, D. E.; Wolverton, C. Structure and diffusion in liquid complex hydrides via ab initio molecular dynamics. *Phys. Rev. B: Condens. Matter Mater. Phys.* **2012**, *86*, 174203.
(75) Arrhenius, S. Über die Dissociationswärme und den Einfluss der Temperatur auf den Dissociationsgrad der Elektrolyte. *Z. Physiol. Chem.* **1889**, *4*, 96−116.
(76) Richards, W. D.; Miara, L. J.; Wang, Y.; Kim, J. C.; Ceder, G. Interface stability in solid-state batteries. *Chem. Mater.* **2016**, *28*, 266−273.
(77) Sun, W.; Dacek, S. T.; Ong, S. P.; Hautier, G.; Jain, A.; Richards, W. D.; Gamst, A. C.; Persson, K. A.; Ceder, G. The thermodynamic scale of inorganic crystalline metastability. *Sci. Adv.* **2016**, *2*, No. e1600225.
(78) Aykol, M.; Dwaraknath, S. S.; Sun, W.; Persson, K. A. Thermodynamic limit for synthesis of metastable inorganic materials. *Sci. Adv.* **2018**, *4*, No. eaaq0148.
(79) Rost, C. M.; Sachet, E.; Borman, T.; Moballegh, A.; Dickey, E. C.; Hou, D.; Jones, J. L.; Curtarolo, S.; Maria, J.-P. Entropy-stabilized oxides. *Nat. Commun.* **2015**, *6*, 8485.
(80) Voskanyan, A. A.; Abramchuk, M.; Navrotsky, A. Entropy Stabilization of TiO_2-Nb_2O_5 Wadsley-Roth Shear Phases and their Prospects for Lithium Ion Battery Anode Materials. *Chem. Mater.* **2020**, *32*, 5301.
(81) Hautier, G.; Ong, S. P.; Jain, A.; Moore, C. J.; Ceder, G. Accuracy of density functional theory in predicting formation energies of ternary oxides from binary oxides and its implication on phase stability. *Phys. Rev. B: Condens. Matter Mater. Phys.* **2012**, *85*, 155208.
(82) Bushick, K.; Hegde, V.; He, J.; Wolverton, C. High-throughput search for novel quaternary oxyarsenides. **2020**, Unpublished work.
(83) Petretto, G.; Gonze, X.; Hautier, G.; Rignanese, G.-M. Convergence and pitfalls of density functional perturbation theory phonons calculations from a high-throughput perspective. *Comput. Mater. Sci.* **2018**, *144*, 331−337.
(84) Gamon, J.; Giaume, D.; Wallez, G.; Labégorre, J.-B.; Lebedev, O. I.; Al Rahal Al Orabi, R.; Haller, S.; Le Mercier, T.; Guilmeau, E.; Maignan, A.; Barboux, P. Substituting Copper with Silver in the BiMOCh Layered Compounds (M= Cu or Ag; Ch= S, Se, or Te): Crystal, Electronic Structure, and Optoelectronic Properties. *Chem. Mater.* **2018**, *30*, 549−558.
(85) BaQais, A.; Curutchet, A.; Ziani, A.; Ait Ahsaine, H.; Sautet, P.; Takanabe, K.; Le Bahers, T. Bismuth Silver Oxysulfide for Photoconversion Applications: Structural and Optoelectronic Properties. *Chem. Mater.* **2017**, *29*, 8679−8689.
(86) Skelton, J. M.; Tiana, D.; Parker, S. C.; Togo, A.; Tanaka, I.; Walsh, A. Influence of the exchange-correlation functional on the quasi-harmonic lattice dynamics of II-VI semiconductors. *J. Chem. Phys.* **2015**, *143*, 064710.
(87) Cassidy, S. J.; Pitcher, M. J.; Lim, J. J. K.; Hadermann, J.; Allen, J. P.; Watson, G. W.; Britto, S.; Chong, E. J.; Free, D. G.; Grey, C. P.; Clarke, S. J. Layered CeSO and LiCeSO Oxide Chalcogenides Obtained via Topotactic Oxidative and Reductive Transformations. *Inorg. Chem.* **2019**, *58*, 3838−3850.
(88) Brothers, E. N.; Izmaylov, A. F.; Normand, J. O.; Barone, V.; Scuseria, G. E. Accurate solid-state band gaps via screened hybrid electronic structure calculations. *J. Chem. Phys.* **2008**, *129*, 011102.
(89) Becke, A. D. A new mixing of Hartree−Fock and local density-functional theories. *J. Chem. Phys.* **1993**, *98*, 1372−1377.
(90) Sambrook, T.; Smura, C. F.; Clarke, S. J.; Ok, K. M.; Halasyamani, P. S. Structure and physical properties of the polar oxysulfide CaZnOS. *Inorg. Chem.* **2007**, *46*, 2571−2574.
(91) Yin, Y.; Tudu, B.; Tiwari, A. Recent advances in oxide thermoelectric materials and modules. *Vacuum* **2017**, *146*, 356−374.
(92) Chen, W.; Pöhls, J.-H.; Hautier, G.; Broberg, D.; Bajaj, S.; Aydemir, U.; Gibbs, Z. M.; Zhu, H.; Asta, M.; Snyder, G. J.; Meredig, B.; White, M. A.; Persson, K.; Jain, A. Understanding thermoelectric properties from high-throughput calculations: trends, insights, and comparisons with experiment. *J. Mater. Chem. C* **2016**, *4*, 4414−4426.
(93) Zhao, L.-D.; He, J.; Berardan, D.; Lin, Y.; Li, J.-F.; Nan, C.-W.; Dragoe, N. BiCuSeO oxyselenides: new promising thermoelectric materials. *Energy Environ. Sci.* **2014**, *7*, 2900−2924.
(94) Snyder, G. J.; Toberer, E. S. *Materials for Sustainable Energy: A Collection of Peer-Reviewed Research and Review Articles from Nature Publishing Group*; World Scientific, 2011; pp 101−110.
(95) Perdew, J. P.; Ruzsinszky, A.; Csonka, G. I.; Vydrov, O. A.; Scuseria, G. E.; Constantin, L. A.; Zhou, X.; Burke, K. Restoring the Density-Gradient Expansion for Exchange in Solids and Surfaces. *Phys. Rev. Lett.* **2008**, *100*, 136406.
(96) Saha, S. K. Exploring the origin of ultralow thermal conductivity in layered BiOCuSe. *Phys. Rev. B: Condens. Matter Mater. Phys.* **2015**, *92*, No. 041202(R).
(97) Ji, H. S.; Togo, A.; Kaviany, M.; Tanaka, I.; Shim, J. H. Low phonon conductivity of layered BiCuOS, BiCuOSe, and BiCuOTe from first principles. *Phys. Rev. B: Condens. Matter Mater. Phys.* **2016**, *94*, 115203.
(98) Pei, Y.; Shi, X.; LaLonde, A.; Wang, H.; Chen, L.; Snyder, G. J. Convergence of electronic bands for high performance bulk thermoelectrics. *Nature* **2011**, *473*, 66.

https://dx.doi.org/10.1021/acs.chemmater.0c01902
Chem. Mater. XXXX, XXX, XXX−XXX

(99) He, J.; Xia, Y.; Naghavi, S. S.; Ozoliņš, V.; Wolverton, C. Designing chemical analogs to PbTe with intrinsic high band degeneracy and low lattice thermal conductivity. *Nat. Commun.* **2019**, *10*, 719.
(100) Zhao, L.-D.; Tan, G.; Hao, S.; He, J.; Pei, Y.; Chi, H.; Wang, H.; Gong, S.; Xu, H.; Dravid, V. P.; Uher, C.; Snyder, G. J.; Wolverton, C. Ultrahigh power factor and thermoelectric performance in hole-doped single-crystal SnSe. *Science* **2016**, *351*, 141−144.
(101) Rowe, D. M. *CRC Handbook of Thermoelectrics*; CRC Press: Boca Raton, 1995; p 11995.
(102) Toberer, E. S.; Zevalkink, A.; Snyder, G. J. Phonon engineering through crystal chemistry. *J. Mater. Chem.* **2011**, *21*, 15843−15852.
(103) Vaqueiro, P.; Al Orabi, R. A. R.; Luu, S. D. N.; Guélou, G.; Powell, A. V.; Smith, R. I.; Song, J.-P.; Wee, D.; Fornari, M. The role of copper in the thermal conductivity of thermoelectric oxychalcogenides: do lone pairs matter? *Phys. Chem. Chem. Phys.* **2015**, *17*, 31735−31740.
(104) Carrete, J.; Mingo, N.; Curtarolo, S. Low thermal conductivity and triaxial phononic anisotropy of SnSe. *Appl. Phys. Lett.* **2014**, *105*, 101907.
(105) Zhao, L.-D.; Lo, S.-H.; Zhang, Y.; Sun, H.; Tan, G.; Uher, C.; Wolverton, C.; Dravid, V. P.; Kanatzidis, M. G. Ultralow thermal conductivity and high thermoelectric figure of merit in SnSe crystals. *Nature* **2014**, *508*, 373−377.
(106) Fortunato, E.; Barquinha, P.; Martins, R. Oxide semiconductor thin-film transistors: a review of recent advances. *Adv. Mater.* **2012**, *24*, 2945−2986.
(107) Varghese, O. K.; Paulose, M.; Grimes, C. A. Long vertically aligned titania nanotubes on transparent conducting oxide for highly efficient solar cells. *Nat. Nanotechnol.* **2009**, *4*, 592.
(108) Yim, K.; Youn, Y.; Lee, M.; Yoo, D.; Lee, J.; Cho, S. H.; Han, S. Computational discovery of p-type transparent oxide semiconductors using hydrogen descriptor. *npj Comput. Mater.* **2018**, *4*, 17.
(109) Sheng, S.; Fang, G.; Li, C.; Xu, S.; Zhao, X. p-type transparent conducting oxides. *Phys. Status Solidi A* **2006**, *203*, 1891−1900.
(110) Banerjee, A. N.; Chattopadhyay, K. K. Recent developments in the emerging field of crystalline p-type transparent conducting oxide thin films. *Prog. Cryst. Growth Charact.* **2005**, *50*, 52−105.
(111) Hautier, G.; Miglio, A.; Ceder, G.; Rignanese, G.-M.; Gonze, X. Identification and design principles of low hole effective mass p-type transparent conducting oxides. *Nat. Commun.* **2013**, *4*, 2292.
(112) Hiramatsu, H.; Kamihara, Y.; Yanagi, H.; Ueda, K.; Kamiya, T.; Hirano, M.; Hosono, H. Layered mixed-anion compounds: Epitaxial growth, active function exploration, and device application. *J. Eur. Ceram. Soc.* **2009**, *29*, 245−253.
(113) Ginley, D. S.; Bright, C. Transparent conducting oxides. *MRS Bull.* **2000**, *25*, 15−18.
(114) Ginley, D. S.; Hosono, H.; Paine, D. C. *Handbook of Transparent Conductors*; Springer, 2010.
(115) Kormath Madam Raghupathy, R.; Wiebeler, H.; Kühne, T. D.; Felser, C.; Mirhosseini, H. Database screening of ternary chalcogenides for p-type transparent conductors. *Chem. Mater.* **2018**, *30*, 6794−6800.
(116) Woods-Robinson, R.; Broberg, D.; Faghaninia, A.; Jain, A.; Dwaraknath, S. S.; Persson, K. A. Assessing high-throughput descriptors for prediction of transparent conductors. *Chem. Mater.* **2018**, *30*, 8375−8389.
(117) Brunin, G.; Ricci, F.; Ha, V.-A.; Rignanese, G.-M.; Hautier, G. Transparent conducting materials discovery using high-throughput computing. *npj Comput. Mater.* **2019**, *5*, 63.
(118) Shi, J.; Cerqueira, T. F.; Cui, W.; Nogueira, F.; Botti, S.; Marques, M. A. High-throughput search of ternary chalcogenides for p-type transparent electrodes. *Sci. Rep.* **2017**, *7*, 43179.
(119) Tarascon, J.-M.; Armand, M. *Materials for Sustainable Energy: A Collection of Peer-Reviewed Research and Review Articles from Nature Publishing Group*; World Scientific, 2011; pp 171−179.
(120) Goodenough, J. B.; Kim, Y. Challenges for rechargeable Li batteries. *Chem. Mater.* **2010**, *22*, 587−603.
(121) Bachman, J. C.; Muy, S.; Grimaud, A.; Chang, H.-H.; Pour, N.; Lux, S. F.; Paschos, O.; Maglia, F.; Lupart, S.; Lamp, P.; Giordano, L.; Shao-Horn, Y. Inorganic solid-state electrolytes for lithium batteries: mechanisms and properties governing ion conduction. *Chem. Rev.* **2016**, *116*, 140−162.
(122) Manthiram, A.; Yu, X.; Wang, S. Lithium battery chemistries enabled by solid-state electrolytes. *Nat. Rev. Mater.* **2017**, *2*, 16103.
(123) Zhao, Q.; Stalin, S.; Zhao, C.-Z.; Archer, L. A. Designing solid-state electrolytes for safe, energy-dense batteries. *Nat. Rev. Mater.* **2020**, *5*, 1−24.
(124) Kamaya, N.; Homma, K.; Yamakawa, Y.; Hirayama, M.; Kanno, R.; Yonemura, M.; Kamiyama, T.; Kato, Y.; Hama, S.; Kawamoto, K.; Mitsui, A. A lithium superionic conductor. *Nat. Mater.* **2011**, *10*, 682.
(125) Banerjee, A.; Park, K. H.; Heo, J. W.; Nam, Y. J.; Moon, C. K.; Oh, S. M.; Hong, S.-T.; Jung, Y. S. Na3SbS4: A Solution Processable Sodium Superionic Conductor for All-Solid-State Sodium-Ion Batteries. *Angew. Chem., Int. Ed.* **2016**, *55*, 9634−9638.
(126) Kato, Y.; Hori, S.; Saito, T.; Suzuki, K.; Hirayama, M.; Mitsui, A.; Yonemura, M.; Iba, H.; Kanno, R. High-power all-solid-state batteries using sulfide superionic conductors. *Nat. Energy* **2016**, *1*, 16030.
(127) Ong, S. P.; Mo, Y.; Richards, W. D.; Miara, L.; Lee, H. S.; Ceder, G. Phase stability, electrochemical stability and ionic conductivity of the $Li_{10\pm1}MP_2X_{12}$ (M= Ge, Si, Sn, Al or P, and X= O, S or Se) family of superionic conductors. *Energy Environ. Sci.* **2013**, *6*, 148−156.
(128) Wenzel, S.; Randau, S.; Leichtweiß, T.; Weber, D. A.; Sann, J.; Zeier, W. G.; Janek, J. Direct observation of the interfacial instability of the fast ionic conductor $Li_{10}GeP_2S_{12}$ at the lithium metal anode. *Chem. Mater.* **2016**, *28*, 2400−2407.
(129) Bruce, P. G.; West, A. R. The A-C Conductivity of Polycrystalline LISICON, $Li_{2+2x}Zn_{1-x}GeO_4$, and a Model for Intergranular Constriction Resistances. *J. Electrochem. Soc.* **1983**, *130*, 662.
(130) Murugan, R.; Thangadurai, V.; Weppner, W. Fast lithium ion conduction in garnet-type $Li_7La_3Zr_2O_{12}$. *Angew. Chem., Int. Ed.* **2007**, *46*, 7778−7781.
(131) He, X.; Zhu, Y.; Mo, Y. Origin of fast ion diffusion in superionic conductors. *Nat. Commun.* **2017**, *8*, 15893.
(132) Kraft, M. A.; Ohno, S.; Zinkevich, T.; Koerver, R.; Culver, S. P.; Fuchs, T.; Senyshyn, A.; Indris, S.; Morgan, B. J.; Zeier, W. G. Inducing High Ionic Conductivity in the Lithium Superionic Argyrodites $Li_{6+x}P_{1-x}Ge_xS_5I$ for All-Solid-State Batteries. *J. Am. Chem. Soc.* **2018**, *140*, 16330−16339.
(133) Doussier-Brochard, C.; Chavillon, B.; Cario, L.; Jobic, S. Synthesis of p-type transparent LaOCuS nanoparticles via soft chemistry. *Inorg. Chem.* **2010**, *49*, 3074−3076.
(134) Stampler, E. S.; Sheets, W. C.; Bertoni, M. I.; Prellier, W.; Mason, T. O.; Poeppelmeier, K. R. Temperature driven reactant solubilization synthesis of BiCuOSe. *Inorg. Chem.* **2008**, *47*, 10009−10016.
(135) Li, M. Q.; Dang, L. Y.; Wang, G. G.; Li, F.; Han, M.; Wu, Z. P.; Li, G. Z.; Liu, Z.; Han, J. C. Bismuth Oxychalcogenide Nanosheet: Facile Synthesis, Characterization, and Photodetector Application. *Adv. Mater. Technol.* **2020**, *5*, 2000180.
(136) Matsumoto, Y.; Yamamoto, T.; Nakano, K.; Takatsu, H.; Murakami, T.; Hongo, K.; Maezono, R.; Ogino, H.; Song, D.; Brown, C. M.; Tassel, C.; Kageyama, H. High-Pressure Synthesis of $A_2NiO_2Ag_2Se_2$ (A= Sr, Ba) with a High-Spin Ni^{2+} in Square-Planar Coordination. *Angew. Chem., Int. Ed.* **2019**, *58*, 756−759.
(137) Persson, K. A.; Waldwick, B.; Lazic, P.; Ceder, G. Prediction of solid-aqueous equilibria: Scheme to combine first-principles calculations of solids with experimental aqueous states. *Phys. Rev. B: Condens. Matter Mater. Phys.* **2012**, *85*, 235438.
(138) Huang, L.-F.; Rondinelli, J. M. Reliable electrochemical phase diagrams of magnetic transition metals and related compounds from

https://dx.doi.org/10.1021/acs.chemmater.0c01902
Chem. Mater. XXXX, XXX, XXX−XXX

high-throughput ab initio calculations. *npj Mater. Degrad.* **2019**, *3*, 1−13.

https://dx.doi.org/10.1021/acs.chemmater.0c01902
Chem. Mater. XXXX, XXX, XXX−XXX